

## 전기전도성 산화주석으로 충전된 폴리(4-메틸-1-펜텐) 나노복합체의 전기적, 열적, 기계적 및 형태학적 특성

구형우 · 김영준<sup>†</sup> · 구진아\* · 정영섭\*\* · 박은수<sup>\*,†</sup>

고려대학교 세종캠퍼스, \*마이크론 테크놀로지, \*\* (주)인테크놀로지  
(2024년 9월 23일 접수, 2024년 12월 4일 수정, 2024년 12월 5일 채택)

## Electrical, Thermal, Mechanical and Morphological Properties of Poly(4-methyl-1-pentene) Nanocomposites Filled with Electrically Conductive Tin Dioxide

Hyung Woo Koo, Young Jun Kim<sup>†</sup>, Anihc Chin A Ku\*, Young Seob Jong\*\*, and Eun-Soo Park<sup>\*,†</sup>

Department of Food and Biotechnology, Korea University Sejong Campus, 2511, Sejong-ro, Jochiwon-eup, Sejong-si 30019, Korea

\*Micron Semiconductor Asia Pte. Ltd., 990 Bendemeer Rd, 339942 Singapore

\*\*Intechology Co., Ltd., 861-46, Poseungjangan-ro, Jang-an-ri, Jangan-myeon, Hwaseong-si, Gyeonggi-do 18586, Korea

(Received September 23, 2024; Revised December 4, 2024; Accepted December 5, 2024)

**초록:** 안티몬이 도핑된 산화주석(ATO)으로 충전된 폴리(4-메틸-1-펜텐)(PMP) 전기전도성 나노복합체를 제작하여 전기적, 열적, 기계적 특성 및 미세구조 연구를 진행하였다. 또한 제작된 PMP/ATO 나노복합체 필름의 전자선 조사에 따른 물성 변화를 비교하였다. 용액 혼합법에 의해 형성된 나노복합체의 퍼콜레이션 임계치는 대략 25 wt%였으며, 이 때의 체적저항 값은  $5.1 \times 10^8 \Omega \cdot \text{cm}$ 을 나타냈다. 전자선 조사량이 증가함에 따라 PMP/ATO 나노복합체의 인장 및 열적 특성은 크게 변했지만 상대적으로 열안정성과 체적저항에는 큰 영향을 미치지 않았다.

**Abstract:** We fabricated electrically conductive nanocomposites consisting of poly(4-methyl-1-pentene) (PMP) filled with antimony-doped tin dioxide (ATO) nanoparticles and investigated their electrical, thermal, mechanical properties, and microstructure. Additionally, the effects of electron beam irradiation on the properties of the prepared PMP/ATO nanocomposite films were compared. The percolation threshold of the nanocomposites formed by the solution-mixing method was about 25 wt%, and the corresponding volume resistivity was  $5.1 \times 10^8 \Omega \cdot \text{cm}$ . With increasing electron beam irradiation dose, the tensile and thermal properties of the PMP/ATO nanocomposites changed significantly, while the thermal stability and volume resistivity were relatively unaffected.

**Keywords:** solution, tin dioxide, nanocomposite, morphology, thermal property.

### Introduction

Anti-static polymer films are crucial for packaging powdered products such as food additives, pharmaceuticals, and cosmetics.<sup>1</sup> By significantly reducing or eliminating static charge, these films prevent powder agglomeration and uneven distribution, ensuring product quality, cleanliness, and safety.<sup>2</sup> Additionally, the packaging material must be suitable for sterilization processes and maintain its integrity post-processing.<sup>3</sup>

Sterilization, a process that eradicates all microorganisms that could contaminate packaging materials and pose a health

risk,<sup>4</sup> is often achieved through radiation treatment in modern mass production.<sup>5</sup> However, controlling unwanted changes in packaging materials, such as deterioration of mechanical properties and discoloration after irradiation, is essential for commercial viability.

The development of radiation-resistant polymer materials could offer a solution to this challenge, as they can withstand typical sterilization doses (1 to 5 Mrad) or even higher doses used in specialized radiation processes.<sup>6,7</sup> To enhance their anti-static and radiation-shielding properties, polymeric materials can be compounded with various fillers.<sup>1,8</sup> Antimony-doped tin oxide (ATO) is a particularly promising filler due to its excellent electrical conductivity and optical transparency.<sup>9</sup> Furthermore, tin's high atomic number and density make it a suitable material for radiation shielding.<sup>8</sup>

<sup>†</sup>To whom correspondence should be addressed.  
yk46@korea.ac.kr, ORCID<sup>®</sup> 0000-0003-1447-7857  
t2phage@hitel.net, ORCID<sup>®</sup> 0000-0002-4150-7401

©2025 The Polymer Society of Korea. All rights reserved.

This study evaluates the electrical, thermal, and mechanical properties of poly(4-methyl-1-pentene) (PMP)/ATO nanocomposites for potential applications in heat-resistant, anti-static films. PMP, a lightweight, high-temperature polyolefin, is renowned for its exceptional acoustic and electrical properties.<sup>10,11</sup> Electro-conductive PMP/ATO nanocomposites with varying ATO content were prepared via a solution-mixing method. Their thermal, mechanical, electrical, and morphological properties were characterized using differential scanning calorimetry (DSC), thermogravimetric analysis (TGA), megohmmeter, X-ray diffraction (XRD), and transmission electron microscopy (TEM). The properties of the prepared nanocomposites were assessed both before and after electron beam (EB) irradiation.

## Experimental

**Materials.** ATO (FS-10P) was generously provided by Ishihara Sangyo Kaisha, Tokyo, Japan. PMP (DX 560M-0) was obtained from Kangshin Industrial Co., Ltd., Seoul, Korea.

**Instrumentation.** The morphology of the ATO nanoparticles was examined using a JEOL JEM-1220 TEM (Tokyo, Japan) operating at an accelerating voltage of 120 kV. The fracture surface morphology of the nanocomposite samples was analyzed using a Hitachi S-4300 SEM (Tokyo, Japan) at an accelerating voltage of approximately 15 kV. XRD analysis was performed using a Rigaku DMAX-2500 diffractometer (Tokyo, Japan) with  $\text{CuK}\alpha$  radiation at room temperature. Tensile testing of dumbbell-shaped specimens (IEC 60811-1-1 type) was conducted at a crosshead speed of 50 mm/min using a DEC-A500TC UTM (Dawha Test Machine, Korea). The thermal properties and thermal stability of the PMP/ATO nanocomposites were determined by the DSC (Perkin-Elmer DSC 7, CT, USA) and TGA (Perkin-Elmer TGA7, CT, USA), respectively. The vol-

ume resistivity ( $V_R$ ) of film samples was calculated using the equation  $V_R = A \cdot R_v / L$  where  $A$  is the effective electrode area ( $\text{cm}^2$ ),  $R_v$  is measured resistance ( $\Omega$ ), and  $L$  is the distance between electrodes (cm). The  $R_v$  of the nanocomposite films ( $8 \text{ cm} \times 1.0 \text{ cm}$ ) was measured using a TeraOhm 5 kV instrument (Metrel, USA) according to ASTM D 257.

**Preparation of PMP/ATO Nanocomposite Film.** PMP resin (30 g) was initially swollen in cyclohexane (970 g) at room temperature for 6 h, followed by stirring at  $60^\circ\text{C}$  for 24 h. ATO (1.67, 3.75, 6.43, 10, and 15 g, corresponding to 10, 20, 30, 40, and 50 wt% ATO, respectively) was added to a flask containing 500 g of a PMP/cyclohexane solution (PMP 15 g, cyclohexane 485 g). The mixture was then subjected to mechanical mixing and bath sonication for 2 h. The resulting PMP/ATO/cyclohexane suspensions, containing 10, 20, 30, 40, and 50 wt% ATO, were used for solvent casting. Each suspension was cast onto a PTFE film-supported surface at room temperature for 24 h. The obtained sheets were dried at  $80^\circ\text{C}$  for 24 h. Film specimens were prepared by pressing the nanocomposites on a plate press at  $260^\circ\text{C}$  for 5 min, followed by rapid immersion in water. Finally, the films were dried at  $100^\circ\text{C}$  for 24 h.

**EB-irradiation of Hot-pressed Film.** PMP and PMP/ATO nanocomposite films were irradiated with EB at room temperature using an ELV 4 accelerator (EB Tech Co., Ltd., Korea) at a rate of 1 m/min. The irradiation dose was varied from 5 to 40 Mrad by adjusting the number of passes. Dose measurements were verified using cellulose triacetate dosimeter film according to ISO/ASTM 51650.

## Results and Discussion

**$V_R$  Changes of PMP/ATO Nanocomposites.** The ATO used in this study was tin dioxide powder coated with a thin

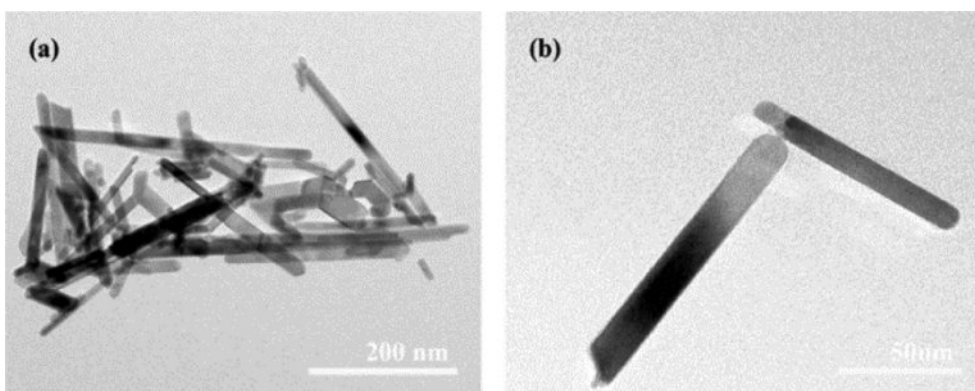


**Figure 1.** TEM micrographs of the ATO nanoparticles.

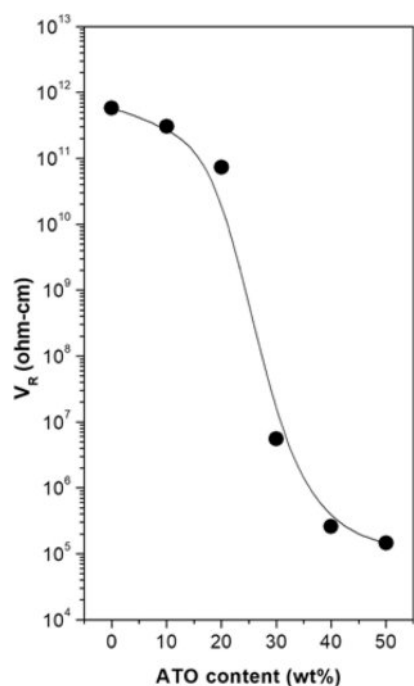


**Figure 2.**  $V_R$  changes of the PMP/ATO nanocomposites with ATO content.

layer of electrically conductive antimony. As shown in Figure 1, it exhibited an acicular shape with a length of  $\sim 500$  nm and a diameter of  $\sim 20$  nm.

Figure 2 illustrates the dependence of  $V_R$  on the ATO content in PMP/ATO nanocomposites. The  $V_R$  decreased significantly with increasing ATO content. When the concentration of electro-conductive particles exceeds the percolation threshold, these particles form a continuous conductive path within the material, enabling electron flow.<sup>12</sup> The percolation threshold for PMP/ATO nanocomposites was estimated to be approximately 25 wt%.

**Tensile Behavior of Nanocomposites.** The tensile properties of PMP/ATO nanocomposites with different ATO contents are summarized in Table 1. The tensile strength (TS) increased up to 10 wt% ATO content but then gradually decreased with further additions. The TS of PMP/ATO10 wt% was 7.7% higher than that of PMP, reaching 15.3 MPa. Conversely, adding 20 wt% ATO decreased the TS by 14.3% compared to the 10 wt% addition. This decrease might be attributed to filler agglomeration, which creates weak points within the nanocomposite.

The elongation at break (EAB) of the nanocomposites gradually decreased with increasing ATO content. For PMP/ATO10 wt% and PMP/ATO50 wt%, the EAB was measured as 364% and 202%, respectively, which were 1.1 and 2.0 times lower than that

**Table 1. Tensile Test Results**

Sample	Tensile properties	
	TS (MPa)	EAB (%)
PMP	$14.2 \pm 0.3$	$404 \pm 14$
PMP/ATO10 wt%	$15.3 \pm 0.7$	$364 \pm 46$
PMP/ATO20 wt%	$13.5 \pm 1.1$	$315 \pm 80$
PMP/ATO30 wt%	$12.8 \pm 1.9$	$291 \pm 51$
PMP/ATO40 wt%	$10.9 \pm 0.9$	$247 \pm 52$
PMP/ATO50 wt%	$9.7 \pm 1.3$	$202 \pm 30$

of PMP. This indicates the filler particles impede the chain mobility of the polymer matrix, reducing its ability to deform.<sup>13,14</sup>

**Morphology of Tensile Fracture Surfaces of Nanocomposites.** A typical tensile fracture surface of an ATO-filled PMP nanocomposite is shown in Figure 3. All nanocomposites exhibited smooth fracture surfaces without necking. While the ATO particles were not directly visible embedded in the PMP matrix, their dispersion state could be inferred from the broken fibers and patterns of the fracture surfaces. When the PMP/ATO melt fills the mold cavity, the mixture melt forms a fountain flow, orienting the ATO particles along the melt direction.<sup>15</sup>

The compositions of PMP/ATO20 wt% and PMP/ATO40 wt% were below and above the percolation threshold, respectively. In the nanocomposite below the percolation threshold (Figure 3(a)), randomly distributed ATO fibers (small white spots) were easily visible, and faint streaks, indicative of potential electrical conductive pathways, began to arrange themselves regularly. As the percolation threshold was reached (Figure 3(b)-top), numerous stripes connected in a canal-like pattern appeared on the tensile fracture surface, indicating that the concentration of ATO fibers was sufficient to maintain conductive pathways.

In the high-magnification SEM image of the fracture surface of PMP/ATO40 wt% (Figure 3(b)-bottom), ATO fibers formed stable conductive pathways connected in a lamellae-like structure. When the ATO content exceeded this level, large barcode-shaped patterns increased on the tensile fracture surface (Figure 3(c)). In this case, the conductive contact points between ATO fibers were saturated, limiting further increases in electrical conductivity of the nanocomposite.

As shown in the XRD pattern of PMP (Figure 4), specific peaks at around  $9.5$ ,  $13.5$ ,  $16.8$ ,  $18.4$ ,  $20.7$ , and  $21.5^\circ$  corresponded to the (200), (201), (212), (321), (400), and (203) crystallographic planes of the Form I orthorhombic phase of PMP.<sup>13,16</sup> Like other semi-crystalline polyolefins, PMP is polymorphic and has five different crystalline forms. Form I is the

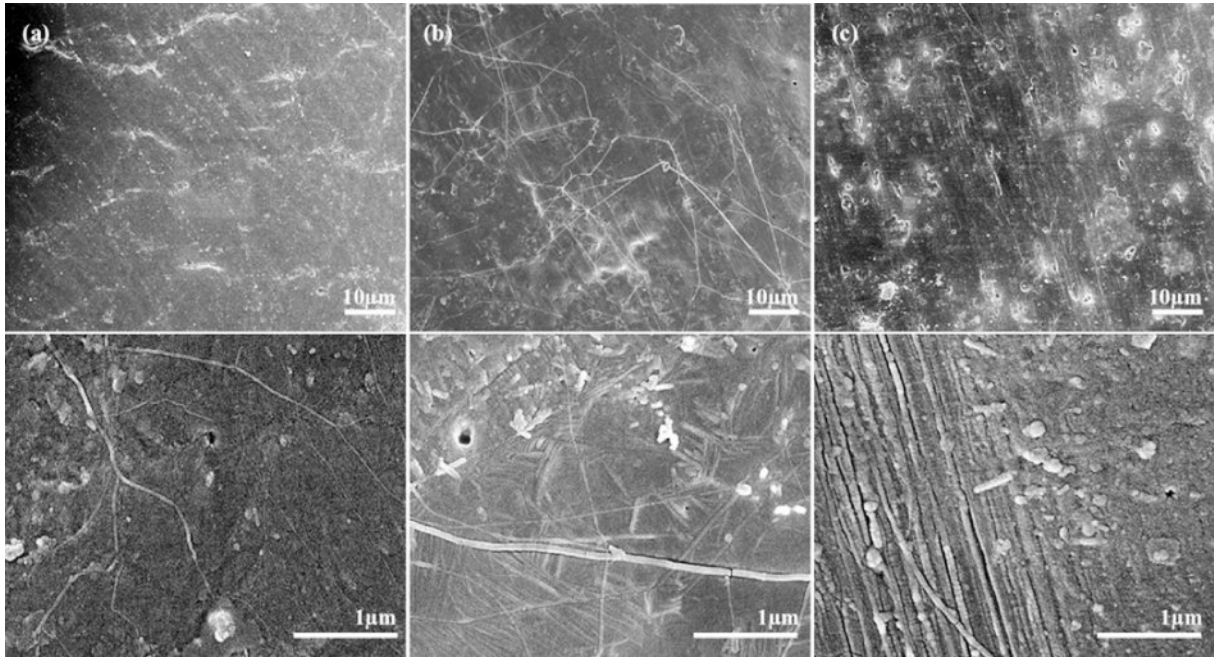


**Figure 3.** Tensile fracture surfaces of the PMP/ATO nanocomposites (ATO content: (a) 20 wt%; (b) 40 wt%; (c) 50 wt%).

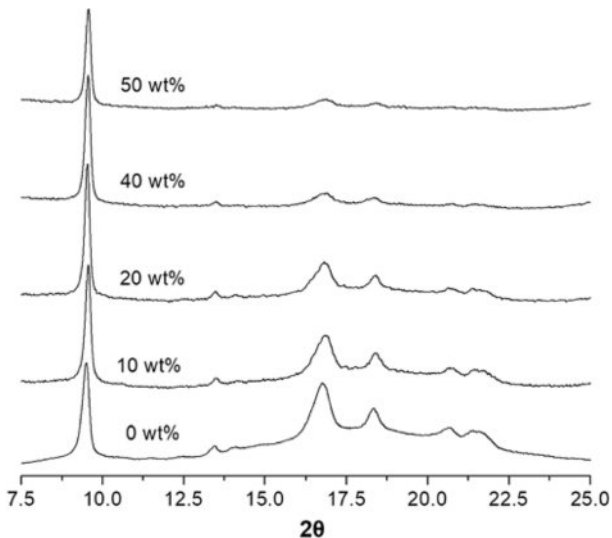


**Figure 4.** XRD patterns of the PMP nanocomposites with ATO content of 0, 10, 20, 40, and 50 wt%.

most stable form, commonly obtained in melt-crystallized samples.<sup>17,18</sup>

All nanocomposite film samples retained the Form I crystal structure. However, the specific diffraction peaks at  $2\theta = 13.5$ ,  $16.8$ ,  $18.4$ ,  $20.7$ , and  $21.5^\circ$  gradually diminished in the XRD curve with increasing ATO content, suggesting that the presence of ATO interfered with the formation of perfect crystals, leading to a decrease in the degree of crystallinity ( $\chi_c$ ) of the nanocomposite.

**DSC Thermal Properties of Nanocomposites.** Figure 5 shows the 1st- and 2nd-scan heating DSC curves of PMP/ATO nanocomposites with varying ATO content. The corresponding thermal data are summarized in Table 2. Pristine PMP exhibited a shoulder peak at  $208.1^\circ\text{C}$  and a broader melting peak at  $218.4^\circ\text{C}$  during the 1st heating scan (Table 2). Similar double melting peak behavior was observed for all PMP/ATO nanocomposites.<sup>19-21</sup> The presence of a single crystalline phase, as confirmed by XRD (Figure 4), suggests that the double melting peaks likely arise from the melting of crystalline regions with different sizes and degrees of perfection.

The addition of ATO up to 30 wt% resulted in the splitting of the 2nd-scan DSC melting peak of PMP (originally at  $220.2^\circ\text{C}$ ) into two peaks: one in the range of  $215$ – $219^\circ\text{C}$  and another around  $223^\circ\text{C}$ . For ATO contents above 40 wt%, the low-temperature peak ( $T_{m21}$ ) almost disappeared, leaving a broad peak nearly identical to that of pristine PMP.

The low-temperature shoulder peak ( $T_{m11}$ ) in the 1st-scan DSC thermogram of PMP almost disappeared in the 2nd-scan DSC thermogram. All samples were prepared through hot-pressing followed by quenching, as described in the experimental section. Therefore, the  $T_{m11}$  peak in the 1st-scan heating curve is likely due to defective crystals initially formed during the quenching process. During the cooling stage, these defective crystals might undergo further crystallization.

The  $T_{m21}$  peak is associated with the melting of metastable

**Table 2.** DSC Thermal Data of the Nanocomposites

Sample	1st-scan <sup>1</sup>			Cooling <sup>2</sup>		2nd-scan <sup>3</sup>		$\chi_c$ (%)
	$T_{m12}$ (°C)	$T_c$ (°C)	$\Delta H_c$ (J/g)	$T_{m21}$ (°C)	$T_{m22}$ (°C)			
PMP	218.4	200.1	6.5	219.2	-		12.6	
PMP/ATO10 wt%	220.0	196.7	8.3	218.4	222.6		11.1	
PMP/ATO20 wt%	221.0	196.4	7.4	216.8	223.1		8.9	
PMP/ATO30 wt%	220.0	195.3	5.2	215.6	223.1		6.8	
PMP/ATO40 wt%	219.6	194.8	4.9	218.6	222.3		4.6	
PMP/ATO50 wt%	219.4	188.9	3.1	218.6	222.1		3.6	

<sup>1</sup>Heating from 20 to 300 °C at a heating rate of 20 °C/min; <sup>2</sup>Cooling to 20 °C at a rate of -10 °C/min; <sup>3</sup>Reheating from 20 to 300 °C at a heating rate of 20 °C/min

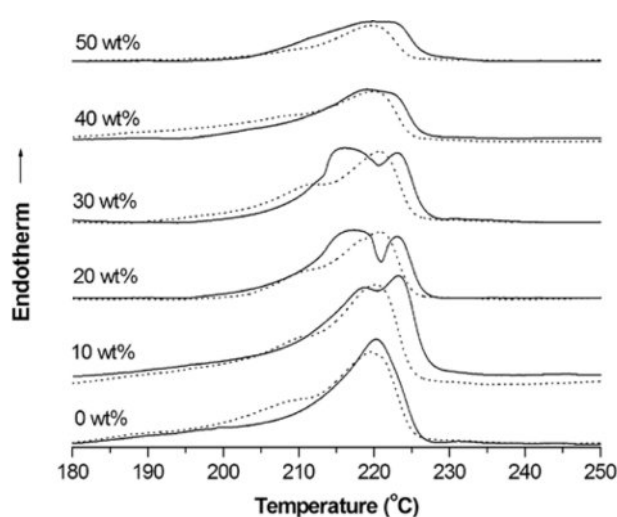


**Figure 5.** DSC thermograms of the PMP nanocomposites with ATO content of 0, 10, 20, 30, 40, and 50 wt% (···: 1st-scan, —: 2nd-scan).

crystals. These crystals likely form during the cooling process as chains segregate and organize into imperfect structures. In contrast, the higher-temperature ( $T_{m22}$ ) peak is attributed to the melting of more perfect crystals. These crystals may arise from a metastable phase segregation process that occurs during the cooling scan, allowing for more ordered structures to form.

The crystallization temperature ( $T_c$ ) and  $\chi_c$  of the nanocomposites significantly decreased with increasing ATO content (Table 2). This could be attributed to the physical hindrance of ATO nanoparticles on crystal growth, as well as potential interference with nucleation or crystal growth mechanisms. Additionally, multiple crystallization peaks appeared when ATO was added (Figure 6, -20, -30 and -40 wt%), suggesting the formation of different morphologies of the same type of crystallite.

**Thermal Stability of Nanocomposites.** Figure 7 shows the TGA traces of the PMP/ATO nanocomposites with ATO contents of 0, 10, 20, 30, 40, and 50 wt%. The shapes of the TGA

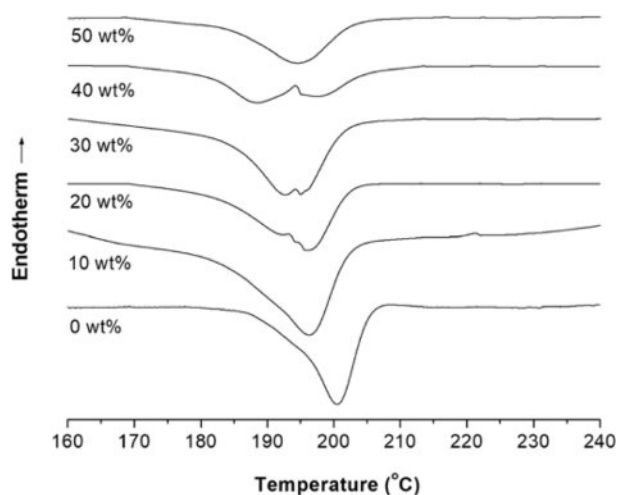


**Figure 6.** DSC cooling curves of the PMP nanocomposites with ATO content of 0, 10, 20, 30, 40, and 50 wt%.

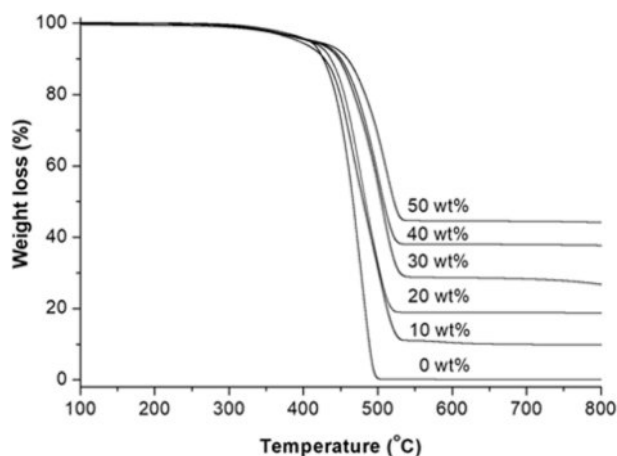


**Figure 7.** TGA traces of the PMP nanocomposites with ATO content of 0, 10, 20, 30, 40, and 50 wt% obtained by scanning from 20 to 800 °C at a heating rate of 20 °C/min under the N<sub>2</sub> atmosphere.

curves indicate that pristine PMP undergoes a one-step weight loss. It retained 99.8% of its initial mass up to approximately

328 °C, at which point it began to decompose. It lost 50% of its initial mass at 467 °C and almost all of its mass at 600 °C, leaving a residue of 0.14%.

For the PMP/ATO nanocomposites, the TGA traces showed a gradual shift in the weight loss towards higher temperatures with increasing ATO content. The temperature at which the nanocomposite sample lost 50% ( $T_{-50\%}$ ) of its initial mass increased with increasing ATO content. The  $T_{-50\%}$  values were 466.1, 479.7, 503.2, 507.1, and 520.7 °C for PMP, PMP/ATO10 wt%, PMP/ATO20 wt%, PMP/ATO30 wt%, PMP/ATO40 wt%, and PMP/ATO50 wt%, respectively. This indicates that the addition of ATO enhances the thermal stability of the nanocomposite system by retarding thermal decomposition. The mineral filler layer might limit the transfer of oxygen and heat, thereby hindering the decomposition process.<sup>22</sup>

**Changes in Physical Properties of PMP/ATO Nanocomposite After EB-irradiation.** Figure 8 summarizes the effect of EB-irradiation on the tensile properties of PMP/ATO nanocomposites. It can be seen that TS (Figure 8(a)) and EAB (Figure 8(b)) of EB-irradiated samples gradually decreased upon EB-irradiation. For nanocomposites irradiated with EB at a dose of 10 Mrad, the changes in TS and EAB were small compared to those of pristine PMP. However, at higher doses, the tensile properties were significantly reduced. For PMP/ATO50 wt%-40M, an approximately 15% and 20% decrease in the TS and EAB of 8.2 MPa and 162%, respectively, was observed relative to those of PMP/ATO50 wt%. The decreased tensile properties of the EB-irradiated samples can be attributed to chain-scission induced by EB-irradiation.<sup>23</sup>

The effect on the EB-irradiation dose on the DSC melting and crystallization behavior of selected samples are shown in Figure 9 and Figure 10, respectively. The 2nd-scan DSC thermogram of the EB-irradiated PMP and PMP/ATO10 wt% exhibited triple endotherms. In contrast, for the EB-irradiated PMP/ATO30 wt% and PMP/ATO50 wt% samples, the lower melting peak disappeared, leaving only two melting peaks.

For EB-irradiated PMP, partially cross-linked chains, chain-scission moieties, and almost pure crystals were observed to coexist.<sup>23</sup> At 10 wt% ATO content, these three crystal structures were not significantly affected. However, when the ATO content increased above 30 wt%, the crystal formation of the partially cross-linked regions appeared to be limited. The reduced mobility of partially cross-linked polymer chains and the presence of a large number of filler particles might hinder the crystallization of polymer molecules in the melt.

Furthermore, increasing EB-irradiation doses led to a decrease

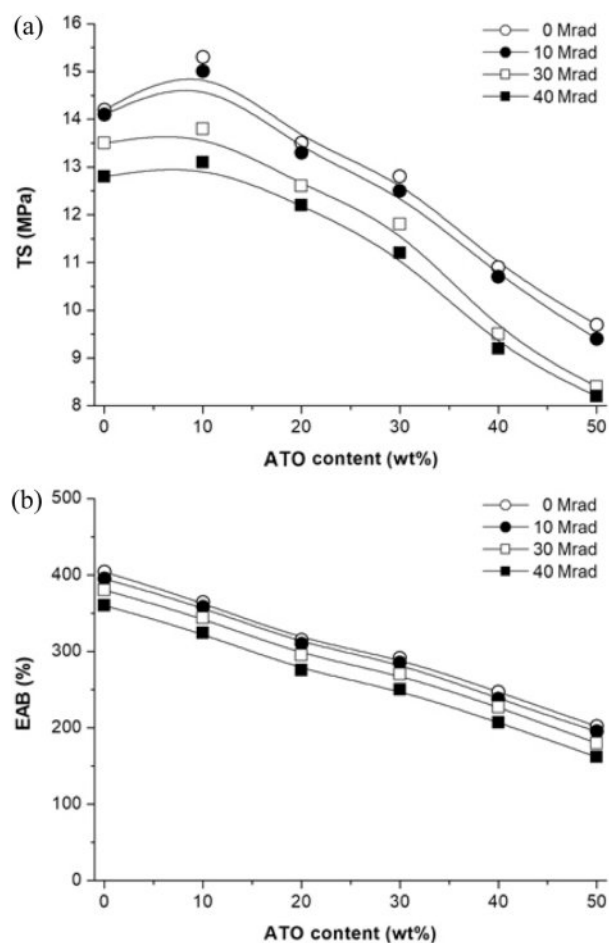


**Figure 8.** Effect of EB irradiation on (a) TS; (b) EAB of the PMP/ATO nanocomposites.

in the peak temperature of both PMP and its nanocomposites. This reduction is likely due to the accumulation of reactive intermediates, such as peroxy radicals and hydroperoxides, induced by irradiation. These intermediates promote chain degradation, resulting in a lower thermal stability.<sup>24,25</sup> This oxidative degradation might produce shorter chains, enhance crystal imperfections, and consequently lower the  $T_m$ .<sup>26,27</sup>

The DSC cooling curves of EB-irradiated PMP and its 10, 30, and 50 wt% ATO-filled PMP nanocomposites are shown in Figure 10. The  $T_c$  of the EB-irradiated PMP and PMP/ATO10 wt% tended to decrease as the EB-irradiation dose increased. For example, the  $T_c$  of pristine PMP decreased from 200.6 to 181.4 °C with increasing EB-irradiation dose. For PMP/ATO30 wt%, it decreases from 196.1 to 180.7 °C.

When radiation damages occur within the crystalline lamellae, they are considered defects. These defects can be removed to the amorphous phase through increased chain folding, lead-

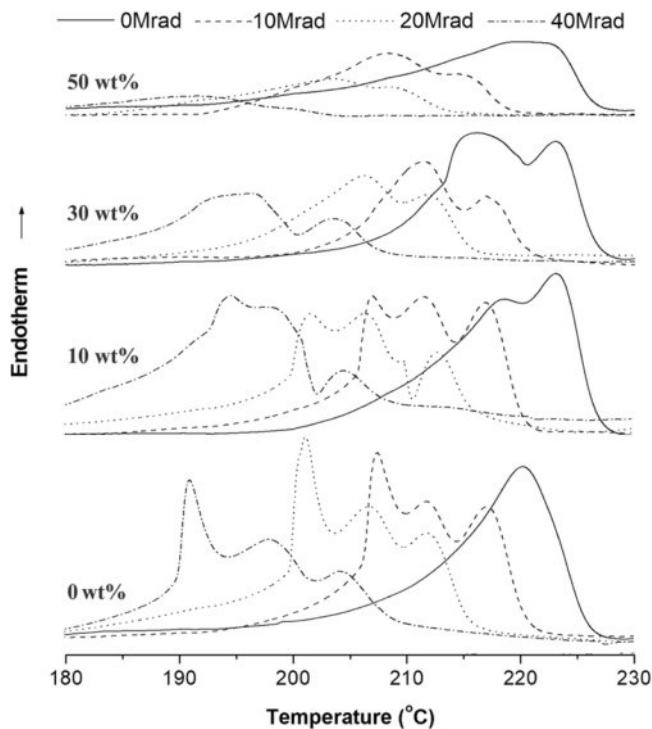


**Figure 9.** 2nd-scan DSC melting thermograms of the PMP, PMP/ATO10 wt%, PMP/ATO30 wt%, and PMP/ATO50 wt% samples before and after EB-irradiation.

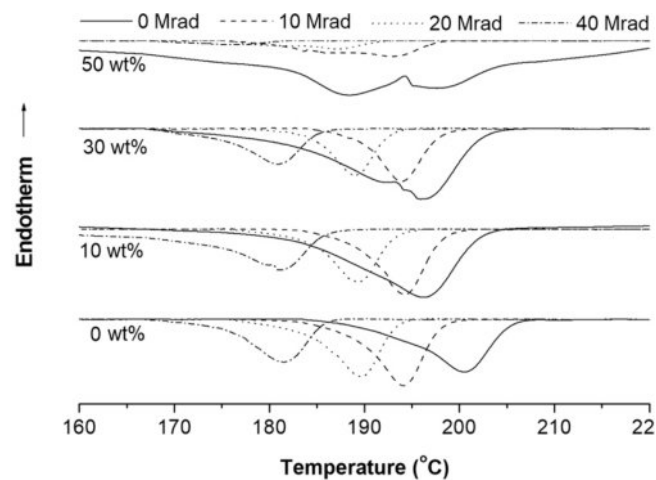


**Figure 10.** Crystallization curves of the PMP, PMP/ATO10 wt%, PMP/ATO30 wt%, and PMP/ATO50 wt% samples before and after EB-irradiation.

ing to a decrease in the original crystalline volume and a corresponding decrease in  $T_c$  values.<sup>27,28</sup>

As shown in Figure 11, the thermal stability of EB-irradiated PMP and PMP/ATO10 wt% films decreased gradually with increasing EB-irradiation dose. The unirradiated PMP/ATO10 wt% exhibited higher thermal-oxidative stability in terms of  $T_{10\%}$

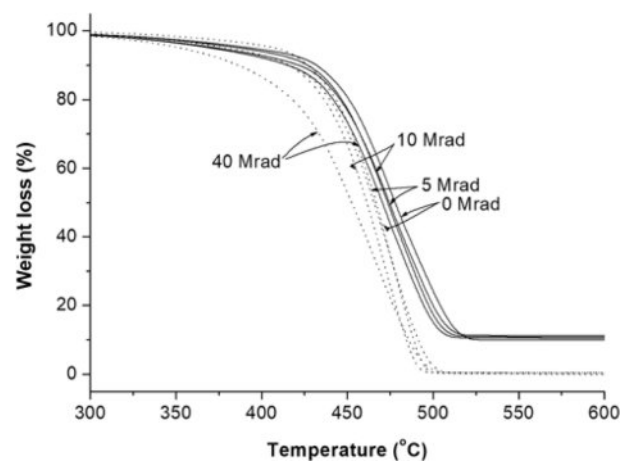


**Figure 11.** TGA traces of the PMP (.....) and PMP/ATO10 wt% nanocomposite (—) before and after EB-irradiation.

compared to the EB-irradiated samples. Additionally, the residues at 470 °C were 62.2, 57.9, 57.0, and 53.0% for PMP/ATO10 wt%, PMP/ATO10 wt%-5M, PMP/ATO10 wt%-10M, and PMP/ATO10 wt%-40M, respectively, confirming that EB-irradiation facilitates thermal degradation. However, the TGA trace of PMP/ATO10 wt%-40M showed a slight shift of the weight loss towards a lower temperature, with stabilization approximately 4 °C lower than that of PMP/ATO10 wt%. In contrast, the TGA trace of PMP under the same conditions showed a shift in weight loss towards lower temperatures by approximately

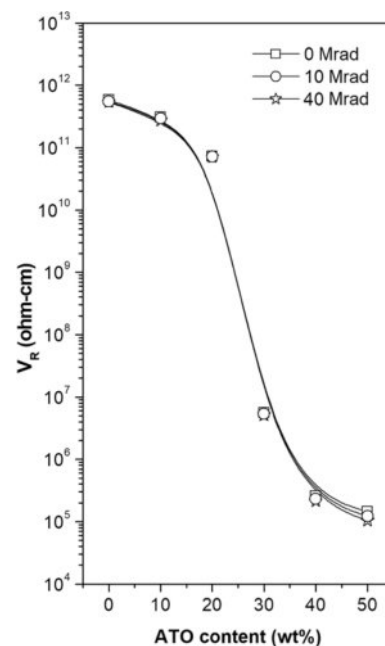


**Figure 12.**  $V_R$  change of the PMP/ATO nanocomposites with EB-irradiation dose.

14 °C. This suggests that the addition of ATO suppresses the chain-scission reaction of PMP caused by strong EB-irradiation.<sup>29</sup>

It was also observed that the  $V_R$  of all nanocomposites did not change significantly with EB-irradiation dose (Figure 12). In partially cross-linked polymer composites, the movement of both polymer molecules and dispersed fillers is restricted, resulting in a more stable conductive pathway.<sup>30,31</sup>

## Conclusions

PMP/ATO nanocomposites were successfully prepared using the solution mixing method. The effects of ATO content on the thermal, mechanical, electrical, and morphological properties of the prepared nanocomposite films were examined. SEM observations revealed that the tensile fracture surface of PMP/ATO nanocomposites gradually changed from faint streaks to canal-like structures and barcode-like patterns with increasing ATO content. This change is attributed to the rearrangement of conductive pathways as ATO content increases.

DSC analysis showed multiple melting and crystallization behaviors in some PMP/ATO nanocomposites. However, XRD analysis confirmed that PMP and PMP/ATO film samples have the same crystal structure, Form I. These results indicated that the multiple melting and crystallization behaviors could be attributed to the formation of two distinct populations of more and less perfect crystals during the cooling process.

Under EB-irradiation of 10 Mrad or less, the tensile properties and thermal stability of PMP/ATO nanocomposites did not change significantly. However, at higher doses, these properties deteriorated sharply. On the other hand, the  $V_R$  of all nanocomposites did not change significantly with EB-irradiation dose due to the more stable conductive pathways formed by the partially cross-linked PMP matrix.

**Conflict of Interest:** The authors declare that there is no conflict of interest.

## References

- Hausmann, K. Permanent Antistatic Agent Offers Long Term Performance for Films and Containers. *Plastics Additives Compounding* **2007**, 9, 40-42.
- Deng, T.; Garg, V.; Bradley, M. S. A. Electrostatic Charging of Fine Powders and Assessment of Charge Polarity Using an Inductive Charge Sensor, *Nanomanufacturing* **2023**, 3, 281-292.
- Jildeh, Z. B.; Wagner, P. H.; Schöning M. J. Sterilization of Objects, Products, and Packaging Surfaces and Their Characterization in Different Fields of Industry: The Status in 2020. *Phys. Status Solidi (A) Appl. Mater. Sci.* **2001**, 218, 2000732.
- Iuliano, A.; Fabiszewska, A.; Kozik, K.; Rzepna, M.; Ostrowska, J.; Dębowski, M.; Plichta, A. Effect of Electron-Beam Radiation and Other Sterilization Techniques on Structural, Mechanical and Microbiological Properties of Thermoplastic Starch Blend. *J. Polym. Environ.* **2021**, 29, 1489-1504.
- Haji-Saeid, M.; Sampa, M. H. O.; Chmielewski, A. G. Radiation Treatment for Sterilization of Packaging Materials. *Radiat. Phys. Chem.* **2007**, 76, 1535-1541.
- Munir, M. T.; Federighi, M. Control of Foodborne Biological Hazards by Ionizing Radiations. *Foods* **2020**, 9, 878.
- Farkas, J.; Mohácsi-Farkas, C. History and Future of Food Irradiation. *Trends Food Sci. Technol.* **2011**, 22, 121-126.
- Chaiphaksa, W.; Yonphan, S.; Kalkomsurapranee, E.; Tuljitrarnom, A.; Kothan S.; Kaewjaeng, S.; Kedkaew, C.; Kaewkhao, J. Photon, Charged Particles, and Neutron Shielding Properties of Natural Rubber/SnO<sub>2</sub> Composites. *Radiat. Phys. Chem.* **2023**, 203, 110622.
- Schumm, B.; Abendroth, T.; Alajlan, S. A.; Almogbel, A. M.; Althues, H.; Härtel, P.; Mäder, G.; Kaskel, S. Combination of Zinc Oxide and Antimony Doped Tin Oxide Nanocoatings for Glazing Application. *Coatings* **2018**, 8, 248.
- Dorigato, A.; Pegoretti, A. Tensile Creep Behaviour of Polymethylpentene-silica Nanocomposites. *Polym. Int.* **2010**, 5, 719-724.
- Choi, Y.-T.; Kim, S. B.; Lee, S. J.; Kim, G.-T.; Park, E.-H.; Park, E. S. Morphology, Thermal, Mechanical and Electrical Insulation Properties of Poly(4-methyl-1-pentene)/poly(ethylene-co-vinyl alcohol)-coated TiO<sub>2</sub> Nanocomposites. *Compos. B: Eng.* **2017**, 114, 268-279.
- Chen, S.; Jin, J.; Zhang, J. Non-isothermal Crystallization Behaviors of Poly(4-methyl-pentene-1). *J. Therm. Anal. Calorim.* **2011**, 103, 229-236.
- Kim, S. B.; Young, S. J.; Park, E.-S. Thermal, Mechanical, Electrical, and Flame Retardant Properties of Poly(4-methyl-1-pentene) Based Composites Filled with Magnesium Hydroxide, *Polym. Korea* **2022**, 46, 529-535.
- Park, E.-S. Mechanical Properties and Processibility of Glass-Fiber, Wollastonite, and Fluoro Rubber-Reinforced Silicone Rubber Composites. *J. Appl. Polym. Sci.* **2007**, 105, 460-468.
- Lei, H. F.; Zhang, Z. Q.; Liu, B. Effect of Fiber Arrangement on Mechanical Properties of Short Fiber Reinforced Composites. *Compos. Sci. Technol.* **2012**, 72, 506-514
- Aharoni, S. M.; Charlet, G.; Delmas, G. Investigation of Solutions and Gels of Poly(4-methyl-1-pentene) in Cyclohexane and Decalin by Viscosimetry, Calorimetry, and X-ray Diffraction. A New Crystalline Form of Poly(4-methyl-1-pentene) from Gels. *Macromol.* **1981**, 1390-1394.
- Fang, J.; Kiran, E. Crystallization and Gelation of Isotactic Poly(4-methyl-1-pentene) in n-pentane and in n-pentane +CO<sub>2</sub> at High Pressures. *J. Supercritical Fluids* **2006**, 38, 132-145.
- Charlet, G.; Delmas, G. Effect of Solvent on the Polymorphism of Poly(4-methylpentene-1): 2. Crystallization in Semi-dilute Solutions. *Polymer* **1984**, 25, 1619-1625.
- Bu, H.; Nie, G.; Rong, J. Crystallization and Compatibility of

- Poly(4-methyl-1-pentene) and Polypropylene in Their Blends. *J. Thermoplastic. Compos. Mater.* **2013**, 28, 1110-1123.
20. Ma, A.-P.; Xu, L.-Y.; Yin, B.; Yang, M.-B.; Xie, B.-H. Influences of Melt-draw Ratio and Annealing on the Crystalline Structure and Orientation of Poly(4-methyl-1-pentene) Casting Films, *RSC Adv.* **2016**, 6, 62038-62044.
  21. Xu, L.-Y.; Yan, H.-W.; Gong, L.; Yin, B.; Yang, M. Poly(4-methyl-1-pentene)/alkylated Graphene Oxide Nanocomposites: the Emergence of a New Crystal Structure. *RSC Adv.* **2015**, 5, 4238-4244.
  22. Sałasińska, K.; Borucka, M.; Celiński, M.; Gajek, A.; Zatorski, W.; Mizera, K.; Leszczyńska, M.; Ryszkowska, J. Thermal Stability, Fire Behavior, and Fumes Emission of Polyethylene Nanocomposites with Halogen-free Fire Retardants. *Adv. Polym. Technol.* **2018**, 37, 2394-2410.
  23. Park, E. S. Effects of Electron Beam Irradiation on Properties of ETFE Insulated Electric Wire. *Iran Polym. J.* **2011**, 20, 873-885.
  24. Otaguro, H.; de Lima, L. F. C. P.; Parra, D. F.; Lugão, A. B.; Chinelatto, M. A.; Canevarolo, S. V. High-energy Radiation Forming Chain Scission and Branching in Polypropylene. *Radiat. Phys. Chem.* **2010**, 79, 318-324.
  25. Narkis, M.; Raiter, I.; Shkolnik, A.; Eyerer, P. J. Structure and Tensile Behavior of Irradiation and Peroxide-crosslinked Polyethylenes. *J. Macromol. Sci. Part B: Physics* **1987**, 26, 37-58.
  26. Park, E. H.; Kim, S. B.; Choi, Y.-T.; Park, E.-S. Effects of Electron Beam Irradiation on Thermal and Mechanical Properties of Nylon 6, Nylon 66 and Nylon 1212. *Res. Rev. Polym.* **2016**, 7, 7-19.
  27. Zaharescu, T.; Silva, L. G. A.; Jipa, S.; Kappel, W. Post-irradiation thermal Degradation of PA6 and PA6,6. *Radiat. Phys. Chem.* **2010**, 79, 388-391.
  28. Zhang, M. C.; Guo, B.-H.; Xu, J. A Review on Polymer Crystallization Theories. *Crystals* **2017**, 7, 4.
  29. Sabet, M.; Soleimani, H.; Hassan, A.; Ratnam, C. T. Electron Beam Irradiation of LDPE Filled with Calcium Carbonate and Metal Hydroxides. *Polym.-Plast. Technol. Eng.* **2014**, 53, 1362-1366.
  30. Chen, L.; Zhang, J. Designs of Conductive Polymer Composites with Exceptional Reproducibility of Positive Temperature Coefficient Effect: A Review. *J. Appl. Polym. Sci.* **2020**, 138, 49677.
  31. Jong, Y. S.; Han, S.-H.; Park, E.-S. Effects of Thermal Aging on Morphology, Resistivity, and Thermal Properties of Extruded High-density Polyethylene/carbon Black Heating Elements. *Polym. Compos.* **2011**, 32, 1049-1061.

**Publisher's Note** The Polymer Society of Korea remains neutral with regard to jurisdictional claims in published articles and institutional affiliations.